CHEMISTRY OF MATERIALS

pubs.acs.org/cm

Article

Methodological Approach to the High-Pressure Synthesis of Nonmagnetic $Li_2B^{4+}B'^{6+}O_6$ Oxides

Mei-Huan Zhao, Chuanhui Zhu, Zhongxiong Sun, Tao Xia, Yifeng Han, Yijie Zeng, Ziyan Gao, Yaping Gong, Xueyun Wang, Jiawang Hong, Wei-Xiong Zhang, Yonggang Wang, Dao-Xin Yao, and Man-Rong Li*

Cite This: *Chem. Mater.* 2022, 34, 186–196

Read Online

ACCESS | Metrics & More | Article Recommendations | Supporting Information

ABSTRACT: High-pressure solid-state synthesis advances boost discoveries of new materials and unusual phenomena but endures stringent recipe conditions, poor yield, and high cost. A methodological approach for accelerated and precisely high-pressure synthesis is therefore highly desired. Here, we take the exotic double-perovskite-related nonmagnetic $Li_2B^{+4}B'^{+6}O_6$ as an example to show the pipeline of data-mining, high-throughput calculations, experimental realization, and chemical interception of metastable phases. A total of 140 compounds in 7 polymorph categories were initially screened by the convex hull, which left ~50% candidates in chemical space on the phase diagram of pressure-dependent polymorph evolution. Li_2TiWO_6 and Li_2TiTeO_6 were singled out for experimental testing according to the predicted map of crystal structure, function, and synthesis parameters. Computation on surface energy effect and interfacial chemical strain suggested that the as-made high-pressure *R*3-Li_2TiTeO_6 polymorph cannot be intercepted below a critical nanoscale but can be stabilized in heterojunction film on a selected compressive substrate at ambient pressure. The developed methodology is expected to accelerate the big-data-driven discovery of generic chemical formula-based new materials beyond perovskites by high-pressure synthesis and shed light on the large-scale stabilization of metastable phases under mild conditions.

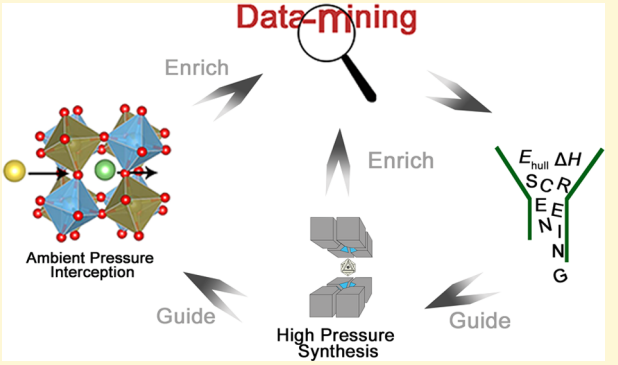

1. INTRODUCTION

Precise prediction of the chemical composition, crystal structure, physical properties, and corresponding preparation parameters of new materials prior to their syntheses is of great importance, especially for those with stringent recipe conditions like high-pressure solid-state synthesis.[1−7] To date, high-throughput projects that integrate computational and experimental data have accelerated actual materials screening at reduced costs,[8] as extensively applied in the exploration of new multifunctional perovskites,[9−11] including dielectrics,[12,13] ferroelectrics,[14−16] piezochromism,[17] photovoltaics,[18,19] and magnetic materials.[20,21] Perovskite is one of the research hotspots in solid-state chemistry and materials sciences, its diverse composition and flexible structures render a rich portfolio of adopting ~90% of the members in the Periodic Table in known compounds.[22−24] As for the conventional ABX_3 (simple) or $A_2BB'X_6$ (double) perovskite structure, the small *B*- and *B*′-cations are octahedrally coordinated to form the framework with the large *A*-cation accommodated in 12-fold AX_{12} cages.[22,25] More than 23 000 compounds have been predicted in the conventional perovskite pool by geometrical descriptors (Goldschmidt tolerance factor *t* together with the new one-dimensional tolerance factor ($\tau \leq$ 4.18) criterion) with claimed accuracy up to 92%,[23,26,27] in which around 2300 compounds have been experimentally observed in the Inorganic Crystal Structure Database (ICSD).[28] In contrast, the emergent exotic perovskite with small *A*-site cations adds new dimensions and enhances the quantum degree of freedom, such as room-temperature multiferroics, colossal magnetoresistance, half-metallicity, and superconductivity with enriched magnetoelectric interplays.[29−31] By theory, there are more than 13 000 compounds in exotic perovskite family through geometrically confined chemical navigation; however, only a very limited number (69) of materials have been reported to date,[32] leaving a vast chemical space for the exploration of new materials. Exotic perovskites are thermodynamically metastable at standard temperature and pressure and mostly needed to be prepared under high-pressure (HP) and high-temperature (HT)

Received: September 4, 2021
Revised: December 7, 2021
Published: December 20, 2021

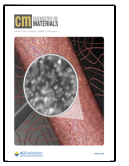

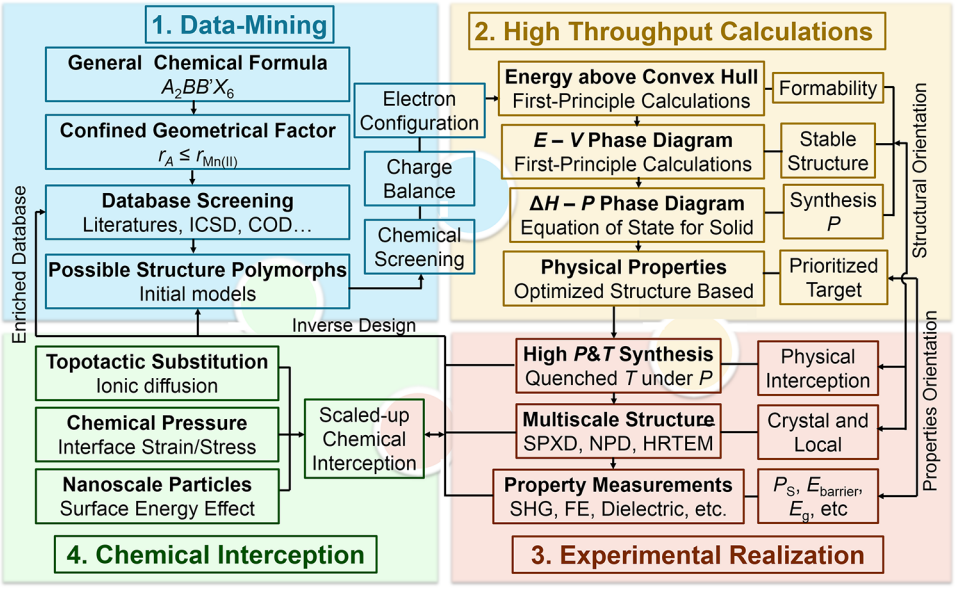

Figure 1. Methodologic workflow of high-pressure solid-state synthesis. (1) Data-mining: data-mining for a given generic chemical formula to dig out possible polymorphs under confinement(s) such as geometric restraints (ionic radius, tolerance factor, distortion, tilting, *etc.*) and defined characters (magnetism, spin−orbit coupling, charge balance, electron configuration, *etc.*), then execute a chemical screening to build initial models for calculations. (2) High-throughput calculations: formation energy convex hull screening in Materials Project before released pressure-dependent polymorph variation calculations to predict the crystal structure, physical properties, and synthesis parameters. (3) Experimental realization: structure and function-oriented precise preparation and physical properties measurements to verify and optimize the calculation parameters for enriched database and inverse design. (4) Chemically intercepting metastable phases: HP polymorph preparation at AP in a scale-up manner at a reduced cost by chemical methods such as chemical pressure, spatial confined nanoparticles, and topotactic substitution.

conditions, by which the metastable phase can be "frozen" by temperature quenching at HP before slow decompression. Unlike conventional perovskites, the geometrical descriptors t and τ are either undistinguishable ($t \sim 0.7-0.8$) or not applicable (exceedingly larger than the critical value of $\tau \sim 4.18$) and thus insufficient for acceptable prediction.[23,26,27,33] The stringent and costly synthesis conditions and poor yield (typically ∼20 mg each batch above 6 GPa) further hinder the discoveries and applications of these appealing materials; therefore, rational design and precise synthesis in an enlarged scale are highly desired.

Experiment based first-principles density functional theory (DFT) calculations, in light of the Murnaghan equation of state for solid,[34] explicitly pinpointed that the phase stability of possible polymorphs can be well evaluated by pressure (P)-dependent evolution of the relative enthalpy (ΔH) or total energy (ΔE), as reported in nonmagnetic $LiSbO_3$, $ZnTiO_3$, and $ZnSnO_3$.[35−37] These findings advanced a new paradigm for computationally assisted identification of new materials by pressure-dependent ΔH calculations over all possible polymorphs in a high-throughput manner. For example, big-data-driven high-throughput calculations (HTC) on exotic double-perovskite-related A_3TeO_6 (A = Mg, Mg, Fe, Co, Ni, Cu, Zn) successfully generated the polymorph-pressure diagram and precisely singled out the HP magnetoelectric $R3$-Co_3TeO_6 for experimental realization.[38]

Because most phase transitions that occur under HP are reversible,[39] retention of the HP phase to ambient pressure (AP) has long been the focus of research. Although temperature quenching at HP in HP-HT synthesis has been widely applied to intercept the metastable phase to AP, the poor yield (∼20 mg per run) hindered further practical applications. Therefore, scaled-up preparation of the metastable phase at ambient or lower pressure is highly desired. Physical (mechanical) pressure effectively reduces the interatomic distances and profoundly compresses the unit cell dimension. Equivalent effect can be induced by chemical pressure, namely, interfacial compressive strain (external chemical pressure) or doping with smaller size ions (internal chemical pressure).[40,41] External chemical pressure has been successfully applied to stabilize the metastable HP phase in heterojunction thin-film form at AP.[42−47] In addition, the surface stress can also produce an effective pressure equivalent to external compression as the size of particles decreases. Therefore, metastable bulk-form HP polymorph could be stabilized at nanoscale below a critical size when the surface energy overwhelms bulk energy.[48−53]

Data-driven and computation-assisted approaches facilitate significant savings in time and cost on HP-HT synthesis. Sequential synthesis of metastable polymorphs by chemical methods is then expected to boost cost-efficiency and large yield for practical applications. However, the compositional identification, precise prediction, and oriented interception entangle full understanding of the possible polymorphs and complicated multidimensional calculations of the chemical and thermodynamic spaces; the metastable phase interception also requires understanding of the multilateral relationship between chemical and physical pressures to rate the experimental limitation. Accordingly, a systematic methodology of HP solid-state synthesis and intercepting metastable polymorphs in chemical ways is highly anticipated, which still remains exceedingly limited and challenging thus far. In this work, we take the exotic perovskite-related nonmagnetic $Li_2B^{+4}B'^{+6}O_6$ as an example, to attentively assess the cationic ordering effect and validate the development of methodologic strategy shown in Figure 1: (1) Data-mining, (2) high-throughput calculations, (3) experimental realization, and (4) chemically intercepting metastable phases. Some compounds in the $Li_2B^{4+}B'^{6+}O_6$

https://doi.org/10.1021/acs.chemmater.1c03073
Chem. Mater. 2022, 34, 186−196

system have been experimentally validated,[54−57] which makes it easier for preliminary computational trial to examine and verify the proposed methods.

2. METHODS AND EXPERIMENTS

2.1. Methods. DFT calculations were performed using the Vienna *Ab initio* Simulation Package (VASP) and the projector-augmented-wave method.[58] Generalized gradient approximation (GGA) implemented in the Perdew−Burke−Ernzerhof (PBE) method was employed for crystal structural optimization.[59] We used plane-wave basis set with a cutoff energy of 700 eV. The Brillouin zone was sampled using a 9 × 9 × 9 Γ-centered *k*-point mesh to produce precise energy for the determination of the energy above the convex hull (E_{hull}) of formation energy[60,61] and Murnaghan equation of state fitting.[34] All of the forces were converged to 0.01 eV/Å. The initially screened compounds by E_{hull} were optimized at a series of constant volumes. The energy−volume (*E*−V) curves were fitted to the Murnaghan equation of state

$$E(V) = B_0V_0\left[\frac{1}{B'(B'-1)}\left(\frac{V_0}{V}\right)^{B'-1} + \frac{V}{B'V_0} - \frac{1}{B'-1}\right] + E_0 \quad (1)$$

where B_0 is the bulk modulus at zero pressure, B' is the first derivative of B_0 with respect to pressure *P*, E_0 is the minimum energy, and V_0 is the volume at minimum energy. The pressure *P*, derived from the combination of the thermodynamic eq 2

$$dE = TdS - PdV \quad (2)$$

where *T* is the temperature, and Murnaghan equation of state can be described as eq 3

$$P = -\left(\frac{\partial E}{\partial V}\right)_S = \frac{B_0}{B'}\left[\left(\frac{V_0}{V}\right)^{B'} - 1\right] \quad (3)$$

The original definition of enthalpy is

$$H = E + PV \quad (4)$$

which makes the enthalpy−pressure (*H*−*P*) function to be

$$H = E_0 + \frac{V_0(P+B_0)}{B'-1}\left(\frac{B_0}{B'P+B_0}\right)^{1/B'} - \frac{B_0V_0}{B'-1} + PV_0\left(\frac{B_0}{B'P+B_0}\right)^{1/B'} \quad (5)$$

By comparing Δ*H* of structures at different pressures, it is thereby possible to figure out the thermodynamically stable structures and the corresponding synthesis parameters or transition points for target phases.

The band structures of the thermodynamically stable compounds were calculated using the HSE06 functional, to provide reasonable accuracy of band gaps for solids.[62] The Ni_3TeO_6-type structures were optimized again with revised PBE for solids (PBEsol), which produces equilibrium volumes and bond lengths more approximate to the experimental values than those from PBE.[63] The secondly optimized structures were used to calculate the normalized bond valence sums (BVS) of Li^+, which were further fitted into the empirical linear function proposed by Ye et al.[64] to estimate the energy barrier ($E_{barrier}$) of ferroelectric reversal. The theoretical spontaneous polarization (P_S) of the polar structures were calculated by point charge model.[65]

The Gibbs free energy (*G*) of a substance can be described as eq 6[52]

$$G(i) = G_B(i) + (6V_m/d)\gamma(i) \quad (6)$$

where G_B is the Gibbs free energy of bulk, γ is the specific surface free energy, V_m is the molar volume, *d* is the particle diameter, and *i* represents the phase type.[48,53,66,67] Equation 6 reveals that it is possible to stabilize the bulk-form metastable phase in nanoscale considering the contribution of significantly enlarged surface area. The surface energy of Li_2TiTeO_6 (LTTO) was calculated with the same parameters as applied in the aforementioned PBE structural optimization. Slabs of 10−12 Å with relaxation layers of 1/3 thickness of slabs were sufficient to be performed with structural optimizations for γ calculations.[68] After obtaining energies of various surfaces, the thermodynamic equilibrium shape of a particle was constituted by Wulff construction[69] to calculate the average surface energy, which were carried out in Wulffpack software.[70]

2.2. Experiments. The AP phase of LTTO was obtained by conventional solid-state reaction using the following raw materials: Li_2CO_3 (99.99%, MACKLIN), TiO_2 (99.99%, MACKLIN), and TeO_2 (99.99%, MACKLIN). Stoichiometric amounts of Li_2CO_3, TiO_2, and TeO_2 were ground to homogeneous mixtures. The powder mixtures were heated up to 600 °C for 12 h in air to fully oxidize Te^{4+} into Te^{6+}, following which the preannealed powders were successively heated (heating rate of 5 °C/min) to 700 and 750 °C for 24 h with an intermediate grinding. All of the above heating treatments were followed by natural cooling to room temperature in the furnace. The AP-synthesized LTTO was then imposed with the pressure of 6 GPa at 850 °C for half an hour to obtain HP-LTTO. The mixture of Li_2WO_4 and TiO_2 was prepared by annealing stoichiometric Li_2CO_3, TiO_2, and WO_3 at 600 and 700 °C for 12 h with an intermediate grinding, successively. Li_2TiWO_6 (LTWO) was synthesized by compressing and heating the preannealed Li_2WO_4 and TiO_2 at 3 GPa and 1000 °C.

HP-LTTO was synthesized in a Walker-type Multi-Anvil Press.[71−73] The compression of Li_2WO_4 and TiO_2 was performed in a single-screw piston cylinder extruder produced by Rocktek. Synchrotron powder X-ray diffraction (SPXD) data were collected at Shanghai Synchrotron Radiation Facility (SSRF) with a wavelength of 0.68993 Å. The data were refined with the Rietveld method using the TOPAS software package.[74] Details data collection and Rietveld refinement are presented in Table S1. Lab powder X-ray diffraction (PXD) data were recorded on a Rigaku MiniFlex 600 equipped with Cu-Kα tube (λ = 1.5418 Å at 40 kV and 15 mA). The differential thermal analysis (DTA) of HP-LTTO was measured up to 800 °C with a heating rate of 10 °C/min in air on an STA 449 F3 Jupiter instrument. The second harmonic generation (SHG) intensities were measured in transmission mode on dense pellets using XPL 1064-200. The UV−vis spectra were recorded on a SHIMADZU, UV-2600. The ferroelectricity was measured by a Precision Premier II (Radiant Technology). The piezoelectric force microscopy (PFM) images were recorded by a scanning probe microscope (Cypher, Asylum Research). To improve PFM sensitivity, we adopted a dual-frequency resonant-tracking technique (DART) provided by Asylum Research Company.

3. RESULTS AND DISCUSSION

3.1. Data-Mining. Previous data-mining for exotic double-perovskite-related $A_2BB'O_6$ and literature adopted six possible polymorphs as initial structural models for calculations,[38,75] from which the ordered-ilmenite (*R*3) structure was excluded to simplify the computations since the ordered-ilmenite structure is very rare in $A_2BB'O_6$.[57] Compared with the Ni_3TeO_6 analogue (*R*3), the *B* and *B*′ sites in the ordered-ilmenite structure are exchanged and can be written as $A_2B'BO_6$. To the best of our knowledge, there are only two ordered-ilmenite-type compounds known to date. Li_2GeTeO_6 is the only one that can be prepared at AP.[57] The ordered-ilmenite-type Mn_2FeMoO_6 cannot be directly prepared, but comes from temperature-induced irreversible cationic rearrangement of the HP-made Ni_3TeO_6-type polymorph upon heating at AP. The low-temperature cationic rearrangement in Mn_2FeMoO_6 was believed to relate with the spin−spin interaction and magnetoelastic effect.[76] The omission of the

https://doi.org/10.1021/acs.chemmater.1c03073
Chem. Mater. 2022, 34, 186−196

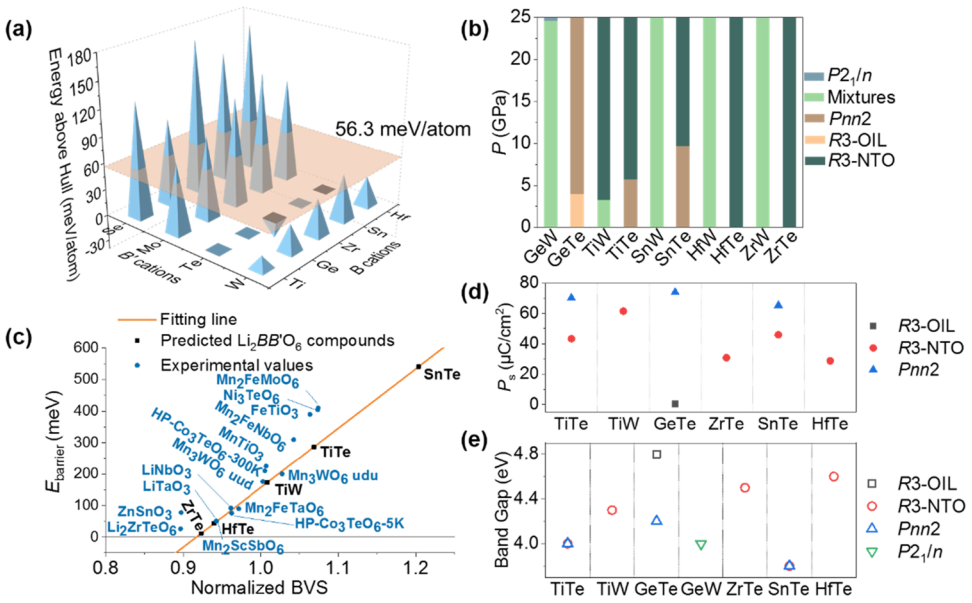

Figure 2. HTC screening results and predicted physical properties. (a) Convex hull screening results, the formation energy of each $Li_2BB'O_6$ is compared to those of all stable crystalline phase of the Li-*B*-*B*′-O phase diagram in Materials Project. (b) Pressure-dependent polymorph map derived from ΔH–P phase diagrams. (c) Energy barriers of ferroelectric reversal of the predicted compounds and the reported experimental results (uud and udu, where "u" stands for "up" and "d" stands for "down", express the magnetic ordering in the primitive cell of Mn_3WO_6) in polar corundum (*R3c and R3*) *derivatives. (d) Theoretical spontaneous polarization. (e) Band gaps calculated by HSE06. In (b)–(e),* $Li_2BB'O_6$ *compounds are labeled as BB′ and OIL and NTO stand for ordered-ilmenite and* Ni_3TeO_6*, respectively, for a concise view.*

ordered-ilmenite polymorph does not seem to diminish the results and conclusions in A_3TeO_6, considering the large charge difference between A^{2+} and Te^{6+} and hence the large energy barrier for anti-site cationic exchange. When it comes to $Li_2B^{4+}B'^{6+}O_6$, the existence of Li_2GeTeO_6 and comparable size and/or charge difference between B^{4+} and B'^{6+} require a comprehensive consideration on cationic arrangement. Therefore, all of the seven possible structural models for small *A*-site $A_2BB'O_6$ known to date are applied to $Li_2B^{4+}B'^{6+}O_6$ (Figure S1 in the Supporting Information).[38,75]

To predict the pressure-dependent polymorph evolution in a given chemical ingredient, the key point is to calculate ΔH variation of each initial structure model upon compressing. The energy scale of ΔH is around 10^{-2}–10^{-1} eV/atom in the reported ΔH–P diagrams of exotic perovskites;[35−37] therefore, the factors (such as temperature and electron-phonon interaction) whose contributions are more than 2 orders of magnitude lower than the energy scale of ΔH can be ignored compared with crystal field, Coulomb repulsion, and pressure effects (10^{-1} to 10^{1} eV).[77,78] The influence of spin–spin interaction (magnetic structure) and spin–orbit coupling (SOC) on ΔH is somehow complicated. Calculations on strong correlated systems such as 4d/5d transition metals containing compounds involve quantum many-body computing and remain a challenge,[79] so a feasible approach is to do validation calculations on known exotic perovskites,[30,31,80−82] to extract common features for inverse design, which is beyond the topic of this work and will be investigated in the future. Magnetic interaction has proven to be critical to determining the ΔH–P phase diagram.[38,75] However, it is by no means an easy job to precisely predict the magnetic structure of an unknown compound.[2,83] Previous findings indicate that calculations of ΔH using proposed colinear magnetic structure(s) may introduce deviation from the real case; nevertheless, it does not affect the overall predicted trend of the ΔH–P phase diagram within the tolerance of error.[38,75] Thus, in $Li_2B^{4+}B'^{6+}O_6$, we only take the cationic arrangements into account, and do not get any magnetic and/or late 4d/5d cations at *B*/*B*′-site to avoid unexpected correlations.

Nonmagnetic and strong SOC metal-free exotic perovskite-related $Li_2B^{4+}B'^{6+}O_6$ enables suitable B^{4+} site of Ge, Sn, Ti, Hf, and Zr and those for B'^{6+} site of Te, Se, Mo, and W over the chemical space restricted by charge balance and geometrical confinement ($0.7 < t < 0.9$).[84] With the combination of all possible compositions, 20 $Li_2B^{4+}B'^{6+}O_6$ (Table S2) were designated to fit into the seven possible structural models (Figure S1), generating 140 (20 × 7) possible compounds, in which ordered-ilmenite-type Li_2GeTeO_6,[57] *Pnn*2-Li_2GeTeO_6 (prepared at 4 GPa), LTTO, Li_2SnTeO_6, and Ni_3TeO_6-type Li_2ZrTeO_6 and Li_2HfTeO_6 have been reported, providing experimental validation of upcoming calculations.

3.2. High-Throughput Calculations. As shown in Figure 1-(2), these chemically screened compounds were initially calculated by DFT and preliminarily screened by E_{hull} for a more predictive and affordable computing, where only the compounds with E_{hull} lower than some thresholds are supposed to be synthesizable.[11,85,86] The compounds predicted to be formable were further calculated on volume variations. The resulting E–V curves were fitted by the Murnaghan equation of state to obtain the relative ΔH–P relationship of various polymorphs and stable decomposition products and thus determine the formation pressures and pressure-dependent phase evolutions. The physical properties, such as band gap (E_g), P_S, and $E_{barrier}$ of the predicted stable or metastable compounds, were further evaluated. The experimental results of selected compounds will inversely enrich the database and guide and optimize the computational methods to produce more accurate outputs in a self-consistent way.

3.2.1. Thermodynamic Screening. The formability of all 140 candidates in $Li_2BB'O_6$ was preliminarily evaluated by

https://doi.org/10.1021/acs.chemmater.1c03073
Chem. Mater. 2022, 34, 186−196

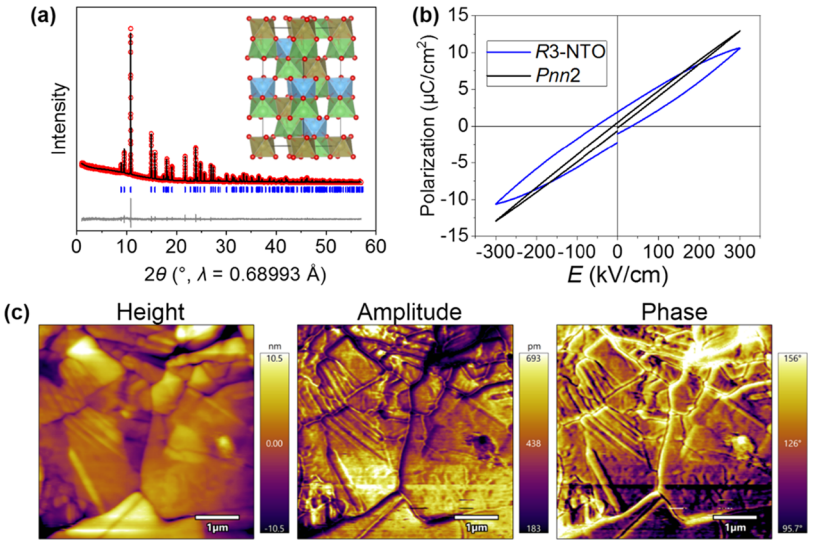

Figure 3. Synthesis and property measurement results of HP-LTTO. (a) Structural refinement results of the HP-LTTO, red circles are observed data, the black line represents the calculated result, blue ticks are peak positions, and the gray line is the difference. (b) *P*−*E* loops of AP and HP-LTTO without observable ferroelectric switching. (c) PFM results on HP-LTTO showing no distinguishable domain switching.

energy distances of the most stable polymorph to the energy convex hulls constituted by the stable compounds approved in Materials Project.[87] $Li_2BB'O_6$, as a quaternary system, is considered to be synthesizable if E_{hull} < 56.3 meV/atom by Sun et al.[88] Detailed calculation results of the 20 $Li_2BB'O_6$ in the space group of the lowest energy and the compounds on the convex hull are listed in Table S2, where the cases with E_{hull} lower than 56.3 meV/atom are highlighted as red. After the above refinements, only compounds with W^{6+} and Te^{6+} in B' sites are supposed to be synthesizable, while the others are too far from the convex hulls to be synthesized as shown in Figure 2a. The compounds with Te^{6+} in B' sites locate on or even below the convex hulls for those with Zr^{4+} or Hf^{4+} in the B sites, which implies that they are thermodynamically stable at AP and 0 K and thus synthesizable, in good agreement with the experimental observation.[54−56] For compounds with W^{6+} in B' sites, their E_{hull} values are less than 56.3 meV/atom, which means that they are metastable at AP and 0 K but possible to stabilize under certain conditions like HP or in nanoscale particles below a critical dimension.

The stable and metastable phases screened by convex hulls were further constrained with structural optimization in a series of constant volumes and the Murnaghan equation of state fittings to figure out their formation and phase transition pressures.[35,37] Figure 2b shows the predicted phase transitions of the stable $Li_2B^{4+}TeO_6$ and metastable $Li_2B^{4+}WO_6$ between 0 and 25 GPa within the pressure range of our large volume Multi-Anvil Press. The detailed phase formations and transitions at various pressures are listed in Table S3. For the stable $Li_2B^{4+}TeO_6$ compounds, Li_2ZrTeO_6 and Li_2HfTeO_6 adopt the same Ni_3TeO_6-type structure throughout the whole pressure range of 0−25 GPa, while the others undergo phase transitions (BB' = GeTe, SnTe, TiTe) as pressure increases. For examples, in LTTO, the *Pnn*2 phase is most stable below 5.7 GPa, above which the ΔH of *R*3 phase becomes lower than that of *Pnn*2 and becomes the most stable phase up to 25 GPa. The predicted *R*3 of ordered-ilmenite-to-*Pnn*2 transition of Li_2GeTeO_6 around 4 GPa is in excellent agreement with previous experimental results.[56] To work out whether the metastable $Li_2B^{4+}WO_6$ compounds are formable among the given pressure range or not, the pressure-dependent ΔH evolution between the targeted compounds in the seven structural models and the stable decomposition compounds on the convex hull along with the metastable phases were compared in Figure S2 as exemplified by LTWO. Pressure-dependent phase evolution of the mixture of Li_2WO_4 and TiO_2 follows the route below: TiO_2 ($C2/m$) + Li_2WO_4 ($R\bar{3}$) → TiO_2 ($I4_1/amd$) + Li_2WO_4 ($I4_1/amd$) → TiO_2 ($Pbcn$) + Li_2WO_4 ($I4_1/amd$) → TiO_2 ($Pbcn$) + Li_2WO_4 ($C2/c$) → TiO_2 ($P2_1/c$) + Li_2WO_4 ($C2/c$). When the enthalpy sums of the above mixture combinations were compared to those of LTWO in different structures (Figure S2c), LTWO seems to be synthesized over 3.3 GPa and adopt the Ni_3TeO_6-type structure until 25 GPa. The other $Li_2B^{4+}WO_6$ compounds were studied the same way. Figure 2b indicates that the $P2_1/n$-Li_2GeWO_6 and Ni_3TeO_6-type LTWO arise over 24.6 and 3.3 GPa, respectively, while the other $Li_2B^{4+}WO_6$ compounds with higher E_{hull} values are unlikely to be synthesizable below 25 GPa.

3.2.2. Physical Properties Prediction. The physical properties of the screened synthesizable compounds were subsequently analyzed. The ferroelectric switching energy barrier ($E_{barrier}$) values for Ni_3TeO_6-type polymorphs were predicted by point charge model,[89] where the normalized BVS of *A* site cations were calculated (Table S4) and fitted into the empirical linear function as shown in Figure 2c and Table S5,[64] where the values of Li_2ZrTeO_6 and Li_2HfTeO_6 are quite approximate to the experimental values. The predicted polar corundum (*R*3*c* and *R*3)-based compounds are theoretically potential ferroelectrics with switchable polarization except for *Pnn*2-Li_2SnTeO_6, $E_{barrier}$ of which is higher than the maximum of the experimentally verified compounds. Figure 2d shows the theoretical polarization for polar structures, and the detailed values are listed in Table S4. Figure 2e and Table S4 present the E_g values calculated by HSE06. All of the screened compounds are insulating, and the E_g value in the same composition follows *Pnn*2 ∼ *R*3-Ni_3TeO_6 < *R*3-ordered-ilmenite. The *Pnn*2 polymorphs have direct band gap, while $P2_1/n$, *R*3- Ni_3TeO_6 and *R*3-ordered-ilmenite polymorphs have indirect band gap. Both the AP and HP phases of LTTO have

https://doi.org/10.1021/acs.chemmater.1c03073
Chem. Mater. 2022, 34, 186−196

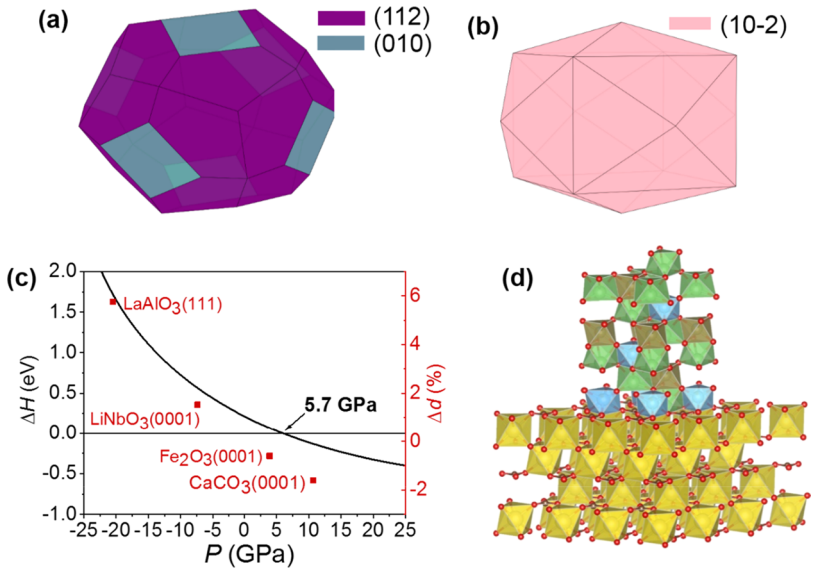

Figure 4. Prediction of chemical stabilization of HP-LTTO at ambient pressure. Surface energy calculation and Wulff construction results of (a) AP-LTTO and (b) HP-LTTO. (c) Comparison of the chemical pressure by interfacial strain on different substrates in the $\Delta H-P$ phase diagram of AP- and HP-LTTO. (d) Scheme of HP-LTTO (upper phase) stabilized by in-plane compressive strain produced by $CaCO_3$ (lower phase), where green, blue, brown, and yellow octahedra stand for LiO_6, TiO_6, TeO_6, and CaO_6 octahedra, and brown and red balls are C and O atoms, respectively.

the same band gap of 4.0 eV, while the band gap of the HP phase is indirect and that of the AP phase is direct. The calculated E_g values of LTTO match well with the experimental UV−vis adsorption spectra shown in Figure S3, validating that HSE06 is suitable for calculating E_g for wide-gap systems.

3.3. Experimental Validation. LTTO, which locates on the convex hull, was predicted to undergo a phase transition from *Pnn*2 to *R*3 around 5.7 GPa. LTWO with a small energy distance to the convex hull lower than 56.3 meV/atom, was taken with LTTO as examples to verify the calculation results and hence provide detailed insights to optimize the structural models and to improve the calculation accuracy for more universal HTC.

3.3.1. Structural and Stability Analyses of AP- and HP-LTTO. The as-synthesized AP-LTTO was examined with PXD measurement as presented in Figure S5c, and no observable impurities were found. The crystal structure of AP-LTTO presented in Figure S4a adopts orthorhombic symmetry (*Pnn*2) derived from $LiSbO_3$, where the edge-sharing SbO_6 octahedral chains construct ion aisles for the occupation of Li^+ ions. As for AP-LTTO, the octahedral chains consist of alternant edge-sharing TiO_6 and TeO_6.[55] Following the workflow in Figure 1-(3), HP-HT synthesis of the nominated LTTO at 6 GPa and 850 °C did yield an HP-*R*3 polymorph as predicted in Figure 2b. The phase purity of HP-LTTO was confirmed by laboratory PXD (Figure S5d). The crystal structure of HP-LTTO was determined by Rietveld refinements on SPXD data shown in Figure 3a and Table S6: Ni_3TeO_6-type structure in the *R*3 space group with lattice parameters of a = 5.06634(2) Å and c = 13.3560(10) Å. The crystal structure of *R*3-LTTO consists of alternated stacking honeycomb-like layers of LiO_6 and TiO_6-TeO_6 octahedra along the c-axis,[90] being isostructural to the reported Li_2ZrTeO_6 (inset of Figure 3a). There exists partial anti-site disordering between Ti and Te, giving the structural formula of $Li_2(Ti_{0.904(7)}Te_{0.096(7)})(Te_{0.88(17)}Ti_{0.12(17)})O_6$. The refinement slightly deviates from the stoichiometry of Li_2TiTeO_6 because of the volatility of the Te element.

Although most HP polymorphs are metastable at standard temperature and pressure, the as-made *R*3-LTTO demonstrates considerable thermal stability at AP. No drastic changes in the heat and mass curves are observed till 750 °C in the DTA curves of *R*3-LTTO (Figure S5a). The thermal resistance to decay was further confirmed by variable-temperature PXD results in Figure S5b, where the HP phase was maintained up to 700 °C. As shown in Figure S5e, most diffraction peaks for HP-LTTO after DTA measurement up to 800 °C can be indexed to TiO_2 ($P4_2/mnm$, ICSD-33838) and Li_2TeO_3 ($C2/c$, ICSD-4317), which indicate decomposition instead of phase transition. Therefore, the pressure-induced phase transition of LTTO is irreversible upon heating at AP.

3.3.2. Synthesis of LTWO. As presented in Figure S6, attempts to prepare a pure phase of LTWO at 3 GPa were unsuccessful according to the prediction as shown in Figures 2a,b and S2. Instead, a mixture of $P4_2/mnm$ TiO_2[91] and orthorhombic Li_2WO_4 phase,[92] whose structure has not yet been solved or included in common database like ICSD and Material Project, was obtained. Considering whether LTWO may be formed or not at higher pressure requires taking orthorhombic Li_2WO_4 into account. Further investigation of the structure of orthorhombic Li_2WO_4 is hence needed to enrich the databases and enhance the calculation precision. On the other hand, TiO_2 and Li_2WO_4 experimentally underwent pressure-dependent structural evolutions, respectively, instead of forming other unexpected phases, which proves the plausibility of the way that the formation pressure could be predicted by evaluating the pressure-dependent enthalpy evolution of the stable compounds located on the convex hull, and the targeted metastable compound as well.

3.3.3. Electrical Properties of HP-R3-LTTO. SHG measurements further corroborate the polar feature of LTTO, where the AP *Pnn*2 phase exhibits a larger P_S than that of the HP polymorph as shown in Figure S7, well echoed with the

https://doi.org/10.1021/acs.chemmater.1c03073
Chem. Mater. 2022, 34, 186−196

calculated results in Table S4. The ferroelectric and PFM measurements are shown in Figure 3b,c. Both the insulating AP and HP phases are robust and did not break down even at an electric field of 300 kV/cm. However, the polarization did not saturate at the maximum electric field and thus no ferroelectric reversal was observed. The PFM results do not distinguish any ferroelectric domains in the polycrystalline specimen either, in contrast to the ferroelectric switching predicted in Figure 2c and Table S5. Further research on single domain film or single crystal is expected to eliminate the grain boundary effect in the future.

3.4. Metastable HP Phase Stabilization by Theory. Data-mining, HTC, and experimental realization following Figure 1-(1)−(3) successfully accelerated structure- and function-oriented discoveries and precise preparation of new compounds. The remaining key issue is to recover the HP polymorph in a scaled-up manner at lower or AP for practical applications. As enumerated in Figure 1-(4), several approaches are possible. Chemical methods, such as external (compressively interfacial strain/stress)[42−47,93−96] and internal (doping with smaller size ions, being equivalent to the formation of a solid solution of the HP phase within adopted (locally) isostructural matrix)[97−100] chemical pressure approaches,[40,41] and spatially confined nanoscale way (surface energy effect), have been experimentally applied to achieve large-scale metastable HP polymorphs at AP. Here, we take the interception of *R*3-LTTO at AP as an example to calculate the proper substrate/lattice orientation and critical size of nanoparticles to guide future experimental work.

3.4.1. Spatial Confined Nanoscale by Surface Energy. Turning bulk materials into nanoscale particles is a feasible way to stabilize the metastable phases under gentle AP conditions as outlined in eq 6.[52] In nanoscale, the surface energy accounts for a large proportion of the total energy originated from the extremely enlarged surface area. If the surface energy of the metastable phase is lower than that of the stable phase, theoretically, the metastable phase will show up at a critical particle size. Calculating surface energy of different polymorphs by DFT can help to figure out whether the surface energy difference would overcome the bulk energy differences, and hence turn the metastable phase to the stable one at the nanoscale or not. For example, Fe_2O_3 and In_2O_3 have been predicted to undergo phase transitions as particle size decreases,[101,102] in good agreement with the experimental results.[50,52] However, as presented in Figure 4a,b, the average surface energy of *R*3-LTTO calculated following Wulff construction is higher than that of the AP *Pnn*2 competitor, suggesting that the HP polymorph is unable to be stabilized via spatially confined nanoscale synthesis. Consequently, we may resort to the other ways in Figure 1-(4) to retain the HP phase, such as applying external chemical pressure in heterojunction film form.

3.4.2. Chemical Pressure by Interfacial Strain. Metastable phase could be stabilized as thin films by tensile or compressive epitaxial strains, namely, chemical pressure produced by interfacial stress.[44,93,103−106] Here, we correlate the lattice mismatch Δd (eq 7) with chemical pressure to stabilize the Ni_3TeO_6-type LTTO along the (0001) orientation on suitable substrates.

$$\Delta d = \frac{d_{\text{substrate}} - d_{\text{film}}}{d_{\text{film}}} \times 100\% \quad (7)$$

where $d_{\text{substrate}}$ and d_{film} are the lattice plane distance of substrates and thin films of targeted compounds, respectively. As shown in Table S7, we consider common (111)-oriented cubic and (0001)-oriented trigonal and hexagonal substrates, all of which adopt threefold in-plane symmetry corresponding to that of (0001)-oriented *R*3-LTTO. For cubic substrates, the trigonal LTTO was first transformed to pseudocubic representation[107] to calculate the lattice mismatch. The in-plane $(2\bar{2}0)$ distance of pseudocubic LTTO at the equilibrium state was compared to $(n\bar{n}0)$ distances of cubic substrates. For trigonal and hexagonal substrates, the in-plane $(10\bar{1}0)$ *R*3-LTTO was directly compared to those of substrates. The detailed comparison results are shown in Table S7. Figure 4c presents the $\Delta H-P$ phase diagram of *R*3- and *Pnn*2-LTTO generated by lattice volume variation around ±25 GPa. As shown in Figures 2b, 3a, and 4c, *Pnn*2-LTTO will transform to the Ni_3TeO_6-type structure over 5.7 GPa. Among all of the substrates in Table S7, only the corresponding lattice of $CaCO_3$ $(R\bar{3}c)$ can generate compressive chemical pressure higher than 5.7 GPa and can be used as a suitable substrate for stabilizing HP-LTTO. It is intriguing to construct Ni_3TeO_6-type LTTO thin film on the (0001)-oriented $CaCO_3$ substrate according to Figure 4c,d in future studies.

4. CONCLUSIONS

Big-data-mining and high-throughput calculations on the screening of nonmagnetic $Li_2BB'O_6$ (*B* = Ge, Ti, Sn, Hf, Zr; *B*′ = Se, Te, W, Mo), confined by thermodynamic formability (convex hull) and pressure-dependent relative enthalpy evolution, successfully singled out the synthesizable Li_2BTeO_6, Li_2GeWO_6, and Li_2TiWO_6 below 25 GPa. Their (meta)stable crystal structures and the corresponding physical properties (band gaps, spontaneous polarization, and energy barriers of ferroelectric reversal) were computed as well. The accuracy of the above predictions is experimentally validated by high-pressure synthesis and characterization of Li_2TiTeO_6, for which the high-pressure polymorph is predicted to be stabilizable in thin film at ambient pressure. However, the synthesis of Li_2TiWO_6 deviated from the predicted results that *R*3 Li_2TiWO_6 will show up over 3.3 GPa. Instead, the orthorhombic Li_2WO_4 beyond consideration was obtained, indicating that databases and initial calculation models need to be enriched and modified by experimental results for further precise predictions. The thermodynamic screening results also suggested that the anti-site *B*-*B*′ exchanging (the ordered-ilmenite structure), which is energetically unfavorable in $Li_2B^{4+}B'^{6+}O_6$ upon pressing, could probably be ignored in future research to save computing power by fixing lower/higher charge cation at the *B*/*B*′ sites, respectively. Our work provides a foundation for further high-throughput calculation of different solid systems such as magnetic compounds, which will lower the experimental trial cost and accelerate the discovery of new materials.

The initial models from confined big-data-mining in Figure 1-(1) may not be fully representative and do not include any possible new structure types that have not been discovered yet, so it is possible to experimentally get unexpected polymorphs, which will enrich the database and add new candidates as initial models for future self-consistent calculations. An alternative approach is to carry out less-supervised calculations to possibly unveil the unknown structure types, which is however less predictive and affordable. It happens that materials computationally predicted to be stable with

https://doi.org/10.1021/acs.chemmater.1c03073
Chem. Mater. 2022, 34, 186−196

encouraging properties cannot be readily realized in the lab, but those with a small positive distance to the hull are obtained. This is understandable since the defects, error of the PBE approximation, and other factors can also lead to corrections to the free energy. Therefore, metastable phases may be left out from the convex hull screening in Figure 1-(2) and depend on further experimental pick-up. The prediction of chemical pressure interception in Figure 1-(4) roughly counts the lattice distortion and does not consider the atomic-scale local structure, which will introduce deviation and need further studies on the calculation models. The surface energy calculation in spatially confined nanoscale interception does not consider the effect from surfactant and/or solvent surroundings and requires further experimental corroboration. Further data accumulation and development of algorithms and machine learning are beneficial to the proposed methodology in this work. We envision that high-pressure solid-state synthesis can be largely accelerated and more predictive and precise in the future.

■ ASSOCIATED CONTENT

Supporting Information

The Supporting Information is available free of charge at https://pubs.acs.org/doi/10.1021/acs.chemmater.1c03073.

Crystal structures of the seven models of exotic perovskite-related system from data-mining (Figure S1); $\Delta H-P$ phase diagrams of LTWO (Figure S2); band structures of AP- and HP-LTTO (Figure S3); comparison of the crystal structures of AP- and HP-LTTO (Figure S4); thermal stability of HP-LTTO (Figure S5); PXD patterns of HP-made "LTWO" (Figure S6); and SHG of AP- and HP-LTTO (Figure S7); thermodynamic information of $Li_2BB'O_6$ (Table S1); predicted structural information of $Li_2BB'O_6$ up to 25 GPa (Table S2); calculated physical properties of screened compounds (Table S3); comparison of the theoretical and experimental $E_{barrier}$ of selected compounds (Table S4); detailed crystallographic information of HP-LTTO (Table S5); and information of substrate candidates to stabilize HP-LTTO via interfacial strain at AP (Table S6) (PDF)

Crystallographic information file for HP-Li_2TiTeO_6 (CIF)

■ AUTHOR INFORMATION

Corresponding Author

Man-Rong Li − *Key Laboratory of Bioinorganic and Synthetic Chemistry of Ministry of Education, School of Chemistry, Sun Yat-Sen University, 510006 Guangzhou, China;* orcid.org/0000-0001-8424-9134; Email: limanrong@mail.sysu.edu.cn

Authors

Mei-Huan Zhao − *Key Laboratory of Bioinorganic and Synthetic Chemistry of Ministry of Education, School of Chemistry, Sun Yat-Sen University, 510006 Guangzhou, China;* orcid.org/0000-0002-3676-3259

Chuanhui Zhu − *Key Laboratory of Bioinorganic and Synthetic Chemistry of Ministry of Education, School of Chemistry, Sun Yat-Sen University, 510006 Guangzhou, China*

Zhongxiong Sun − *Key Laboratory of Bioinorganic and Synthetic Chemistry of Ministry of Education, School of Chemistry, Sun Yat-Sen University, 510006 Guangzhou, China*

Tao Xia − *Key Laboratory of Bioinorganic and Synthetic Chemistry of Ministry of Education, School of Chemistry, Sun Yat-Sen University, 510006 Guangzhou, China*

Yifeng Han − *Key Laboratory of Bioinorganic and Synthetic Chemistry of Ministry of Education, School of Chemistry, Sun Yat-Sen University, 510006 Guangzhou, China*

Yijie Zeng − *School of Science, Hangzhou Dianzi University, Hangzhou 310018, China*

Ziyan Gao − *School of Aerospace Engineering, Beijing Institute of Technology, Beijing 100081, China*

Yaping Gong − *Key Laboratory of Bioinorganic and Synthetic Chemistry of Ministry of Education, School of Chemistry, Sun Yat-Sen University, 510006 Guangzhou, China*

Xueyun Wang − *School of Aerospace Engineering, Beijing Institute of Technology, Beijing 100081, China;* orcid.org/0000-0001-5264-9539

Jiawang Hong − *School of Aerospace Engineering, Beijing Institute of Technology, Beijing 100081, China;* orcid.org/0000-0002-9915-8072

Wei-Xiong Zhang − *Key Laboratory of Bioinorganic and Synthetic Chemistry of Ministry of Education, School of Chemistry, Sun Yat-Sen University, 510006 Guangzhou, China;* orcid.org/0000-0003-0797-3465

Yonggang Wang − *Center for High Pressure Science and Technology Advanced Research (HPSTAR), Beijing 100094, China;* orcid.org/0000-0003-4816-9182

Dao-Xin Yao − *School of Physics, Sun Yat-Sen University, 510275 Guangzhou, China*

Complete contact information is available at: https://pubs.acs.org/10.1021/acs.chemmater.1c03073

Notes

The authors declare no competing financial interest.

■ ACKNOWLEDGMENTS

This work was financially supported by the National Natural Science Foundation of China (NSFC-22090041, 21875287, 21801253, 11804404, 11874400, and 22071273), National Key R&D Program of China (2018YFA0305700 and 2019YFA0307900), the Program for Guangdong Introducing Innovative and Entrepreneurial Teams (2017ZT07C069), the Key Research Program of Frontier Sciences of the Chinese Academy of Sciences (QYZDB-0S0S0W0-SLH013), and the CAS Interdisciplinary Innovation Team. Z.G. and X.W. acknowledge the Beijing Natural Science Foundation (grant no. Z190011) and the Beijing Institute of Technology Research Fund Program for Young Scholars. The authors thank Prof. David Walker at LDEO of Columbia University for useful discussions, beamline BL14B1 (SSRF) for providing the beam time, and the National Supercomputer Center in Guangzhou.

■ REFERENCES

(1) Court, C. J.; Cole, J. M. Magnetic and superconducting phase diagrams and transition temperatures predicted using text mining and machine learning. *npj Comput. Mater.* **2020**, *6*, No. 18.

(2) Alberi, K.; Nardelli, M. B.; Zakutayev, A.; Mitas, L.; Curtarolo, S.; Jain, A.; Fornari, M.; Marzari, N.; Takeuchi, I.; Green, M. L.; Kanatzidis, M.; Toney, M. F.; Butenko, S.; Meredig, B.; Lany, S.;

Kattner, U.; Davydov, A.; Toberer, E. S.; Stevanovic, V.; Walsh, A.; Park, N.-G.; Aspuru-Guzik, A.; Tabor, D. P.; Nelson, J.; Murphy, J.; Setlur, A.; Gregoire, J.; Li, H.; Xiao, R.; Ludwig, A.; Martin, L. W.; Rappe, A. M.; Wei, S.-H.; Perkins, J. The 2019 materials by design roadmap. *J. Phys. D: Appl. Phys.* **2018**, *52*, No. 013001.
(3) Louie, S. G.; Chan, Y.-H.; da Jornada, F. H.; Li, Z.; Qiu, D. Y. Discovering and understanding materials through computation. *Nat. Mater.* **2021**, *20*, 728−735.
(4) Friederich, P.; Häse, F.; Proppe, J.; Aspuru-Guzik, A. Machine-learned potentials for next-generation matter simulations. *Nat. Mater.* **2021**, *20*, 750−761.
(5) Tripathi, M. K.; Kumar, R.; Tripathi, R. Big-data driven approaches in materials science: A survey. *Mater. Today: Proc.* **2020**, *26*, 1245−1249.
(6) Olson, G. B. Designing a new material world. *Science* **2000**, *288*, 993.
(7) Xiang, X. D.; Sun, X.; Briceño, G.; Lou, Y.; Wang, K.-A.; Chang, H.; Wallace-Freedman, W. G.; Chen, S.-W.; Schultz, P. G. A combinatorial approach to materials discovery. *Science* **1995**, *268*, 1738.
(8) Cole, J. M. A design-to-device pipeline for data-driven materials discovery. *Acc. Chem. Res.* **2020**, *53*, 599−610.
(9) Balachandran, P. V.; Emery, A. A.; Gubernatis, J. E.; Lookman, T.; Wolverton, C.; Zunger, A. Predictions of new ABO_3 perovskite compounds by combining machine learning and density functional theory. *Phys. Rev. Mater.* **2018**, *2*, No. 043802.
(10) Emery, A. A.; Wolverton, C. High-throughput DFT calculations of formation energy, stability and oxygen vacancy formation energy of ABO_3 perovskites. *Sci. Data* **2017**, *4*, No. 170153.
(11) Wang, H.-C.; Schmidt, J.; Botti, S.; Marques, M. A. L. A high-throughput study of oxynitride, oxyfluoride and nitrofluoride perovskites. *J. Mater. Chem. A* **2021**, *9*, 8501−8513.
(12) Kim, C.; Pilania, G.; Ramprasad, R. Machine learning assisted predictions of intrinsic dielectric breakdown strength of ABX_3 perovskites. *J. Phys. Chem. C* **2016**, *120*, 14575−14580.
(13) Choudhary, K.; Garrity, K. F.; Sharma, V.; Biacchi, A. J.; Hight Walker, A. R.; Tavazza, F. High-throughput density functional perturbation theory and machine learning predictions of infrared, piezoelectric, and dielectric responses. *npj Comput. Mater.* **2020**, *6*, No. 64.
(14) Min, K.; Cho, E. Accelerated discovery of potential ferroelectric perovskite via active learning. *J. Mater. Chem. C* **2020**, *8*, 7866−7872.
(15) Zhai, X.; Chen, M.; Lu, W. Accelerated search for perovskite materials with higher Curie temperature based on the machine learning methods. *Comput. Mater. Sci.* **2018**, *151*, 41−48.
(16) Balachandran, P. V.; Kowalski, B.; Sehirlioglu, A.; Lookman, T. Experimental search for high-temperature ferroelectric perovskites guided by two-step machine learning. *Nat. Commun.* **2018**, *9*, No. 1668.
(17) Majumdar, A.; Adeleke, A. A.; Chakraborty, S.; Ahuja, R. Emerging piezochromism in lead free alkaline earth chalcogenide perovskite $AZrS_3$ (*A* = Mg, Ca, Sr and Ba) under pressure. *J. Mater. Chem. C* **2020**, *8*, 16392−16403.
(18) Im, J.; Lee, S.; Ko, T.-W.; Kim, H. W.; Hyon, Y.; Chang, H. Identifying Pb-free perovskites for solar cells by machine learning. *npj Comput. Mater.* **2019**, *5*, No. 37.
(19) Kuhar, K.; Crovetto, A.; Pandey, M.; Thygesen, K. S.; Seger, B.; Vesborg, P. C. K.; Hansen, O.; Chorkendorff, I.; Jacobsen, K. W. Sulfide perovskites for solar energy conversion applications: computational screening and synthesis of the selected compound $LaYS_3$. *Energy Environ. Sci.* **2017**, *10*, 2579−2593.
(20) Halder, A.; Ghosh, A.; Dasgupta, T. S. Machine-learning-assisted prediction of magnetic double perovskites. *Phys. Rev. Mater.* **2019**, *3*, No. 084418.
(21) Cai, Y.; Wei, Y.; Ming, X.; Du, F.; Meng, X.; Wang, C.; Chen, G. Prediction of the phase transition from ferromagnetic perovskite to non-magnetic post-perovskite in $SrRuO_3$: A first-principles study. *Solid State Commun.* **2011**, *151*, 798−801.
(22) Vasala, S.; Karppinen, M. $A_2B'B''O_6$ perovskites: A review. *Prog. Solid State Chem.* **2015**, *43*, 1−36.
(23) Filip, M. R.; Giustino, F. The geometric blueprint of perovskites. *Proc. Natl. Acad. Sci. U.S.A.* **2018**, *115*, 5397.
(24) Peña, M. A.; Fierro, J. L. G. Chemical structures and performance of perovskite oxides. *Chem. Rev.* **2001**, *101*, 1981−2018.
(25) King, G.; Woodward, P. M. Cation ordering in perovskites. *J. Mater. Chem.* **2010**, *20*, 5785−5796.
(26) Sun, Q.; Yin, W.-J. Thermodynamic stability trend of cubic perovskites. *J. Am. Chem. Soc.* **2017**, *139*, 14905−14908.
(27) Bartel, C. J.; Sutton, C.; Goldsmith, B. R.; Ouyang, R.; Musgrave, C. B.; Ghiringhelli, L. M.; Scheffler, M. New tolerance factor to predict the stability of perovskite oxides and halides. *Sci. Adv.* **2019**, *5*, No. eaav0693.
(28) Belsky, A.; Hellenbrandt, M.; Karen, V. L.; Luksch, P. New developments in the Inorganic Crystal Structure Database (ICSD): accessibility in support of materials research and design. *Acta Crystallogr., Sect. B: Struct. Sci.* **2002**, *58*, 364−369.
(29) Li, M.-R.; Retuerto, M.; Walker, D.; Sarkar, T.; Stephens, P. W.; Mukherjee, S.; Dasgupta, T. S.; Hodges, J. P.; Croft, M.; Grams, C. P.; Hemberger, J.; Sánchez-Benítez, J.; Huq, A.; Saouma, F. O.; Jang, J. I.; Greenblatt, M. Magnetic-structure-stabilized polarization in an above-room-temperature ferrimagnet. *Angew. Chem., Int. Ed.* **2014**, *53*, 10774−10778.
(30) Li, M.-R.; Retuerto, M.; Deng, Z.; Stephens, P. W.; Croft, M.; Huang, Q.; Wu, H.; Deng, X.; Kotliar, G.; Sánchez-Benítez, J.; Hadermann, J.; Walker, D.; Greenblatt, M. Giant magnetoresistance in the half-metallic double-perovskite ferrimagnet Mn_2FeReO_6. *Angew. Chem., Int. Ed.* **2015**, *54*, 12069−12073.
(31) Arévalo-López, A. M.; McNally, G. M.; Attfield, J. P. Large magnetization and frustration switching of magnetoresistance in the double-perovskite ferrimagnet Mn_2FeReO_6. *Angew. Chem., Int. Ed.* **2015**, *54*, 12074−12077.
(32) Alexei, A. B.; Wei, Y. High-pressure synthesis, crystal chemistry and physics of perovskites with small cations at the A site. *J. Phys.: Condens. Matter* **2014**, *26*, No. 163201.
(33) Hossain, A.; Bandyopadhyay, P.; Roy, S. An overview of double perovskites $A_2B'B''O_6$ with small ions at *A* site: Synthesis, structure and magnetic properties. *J. Alloys Compd.* **2018**, *740*, 414−427.
(34) Murnaghan, F. D. The compressibility of media under extreme pressures. *Proc. Natl. Acad. Sci. U.S.A.* **1944**, *30*, 244−247.
(35) Inaguma, Y.; Aimi, A.; Shirako, Y.; Sakurai, D.; Mori, D.; Kojitani, H.; Akaogi, M.; Nakayama, M. High-pressure synthesis, crystal structure, and phase stability relations of a $LiNbO_3$-type polar titanate $ZnTiO_3$ and its reinforced polarity by the second-order Jahn−Teller effect. *J. Am. Chem. Soc.* **2014**, *136*, 2748−2756.
(36) Nakayama, M.; Nogami, M.; Yoshida, M.; Katsumata, T.; Inaguma, Y. First-principles studies on novel polar oxide $ZnSnO_3$; pressure-induced phase transition and electric properties. *Adv. Mater.* **2010**, *22*, 2579−2582.
(37) Inaguma, Y.; Aimi, A.; Mori, D.; Katsumata, T.; Ohtake, M.; Nakayama, M.; Yonemura, M. High-pressure synthesis, crystal ctructure, chemical bonding, and ferroelectricity of $LiNbO_3$-type $LiSbO_3$. *Inorg. Chem.* **2018**, *57*, 15462−15473.
(38) Han, Y.; Wu, M.; Gui, C.; Zhu, C.; Sun, Z.; Zhao, M.-H.; Savina, A. A.; Abakumov, A. M.; Wang, B.; Huang, F.; He, L.; Chen, J.; Huang, Q.; Croft, M.; Ehrlich, S.; Khalid, S.; Deng, Z.; Jin, C.; Grams, C. P.; Hemberger, J.; Wang, X.; Hong, J.; Adem, U.; Ye, M.; Dong, S.; Li, M.-R. Data-driven computational prediction and experimental realization of exotic perovskite-related polar magnets. *npj Quantum Mater.* **2020**, *5*, No. 92.
(39) Xiao, G.; Wang, K.; Zhu, L.; Tan, X.; Qiao, Y.; Yang, K.; Ma, Y.; Liu, B.; Zheng, W.; Zou, B. Pressure-induced reversible phase transformation in nanostructured Bi_2Te_3 with reduced transition pressure. *J. Phys. Chem. C* **2015**, *119*, 3843−3848.
(40) Fournier, J.-M. Chemical pressure in actinide systems. *Phys. B* **1993**, *190*, 50−54.
(41) Dawley, N. M.; Marksz, E. J.; Hagerstrom, A. M.; Olsen, G. H.; Holtz, M. E.; Goian, V.; Kadlec, C.; Zhang, J.; Lu, X.; Drisko, J. A.;

Uecker, R.; Ganschow, S.; Long, C. J.; Booth, J. C.; Kamba, S.; Fennie, C. J.; Muller, D. A.; Orloff, N. D.; Schlom, D. G. Targeted chemical pressure yields tuneable millimetre-wave dielectric. *Nat. Mater.* **2020**, *19*, 176−181.
(42) Zhang, L.; Chen, J.; Fan, L.; Diéguez, O.; Cao, J.; Pan, Z.; Wang, Y.; Wang, J.; Kim, M.; Deng, S.; Wang, J.; Wang, H.; Deng, J.; Yu, R.; Scott, J. F.; Xing, X. Giant polarization in super-tetragonal thin films through interphase strain. *Science* **2018**, *361*, 494.
(43) Shi, G.; Chen, L.; Yang, Y.; Li, D.; Qian, Z.; Liang, S.; Yan, L.; Li, L. H.; Wu, M.; Fang, H. Two-dimensional Na−Cl crystals of unconventional stoichiometries on graphene surface from dilute solution at ambient conditions. *Nat. Chem.* **2018**, *10*, 776−779.
(44) Son, J. Y.; Lee, G.; Jo, M.-H.; Kim, H.; Jang, H. M.; Shin, Y.-H. Heteroepitaxial ferroelectric $ZnSnO_3$ thin film. *J. Am. Chem. Soc.* **2009**, *131*, 8386−8387.
(45) Li, M.-R.; Adem, U.; McMitchell, S. R. C.; Xu, Z.; Thomas, C. I.; Warren, J. E.; Giap, D. V.; Niu, H.; Wan, X.; Palgrave, R. G.; Schiffmann, F.; Cora, F.; Slater, B.; Burnett, T. L.; Cain, M. G.; Abakumov, A. M.; van Tendeloo, G.; Thomas, M. F.; Rosseinsky, M. J.; Claridge, J. B. A polar corundum oxide displaying weak ferromagnetism at room temperature. *J. Am. Chem. Soc.* **2012**, *134*, 3737−3747.
(46) Gich, M.; Fina, I.; Morelli, A.; Sánchez, F.; Alexe, M.; Gàzquez, J.; Fontcuberta, J.; Roig, A. Multiferroic iron oxide thin films at room temperature. *Adv. Mater.* **2014**, *26*, 4645−4652.
(47) Rao, B. N.; Yasui, S.; Han, Y.; Hamasaki, Y.; Katayama, T.; Shiraishi, T.; Kiguchi, T.; Itoh, M. Redox-based multilevel resistive switching in $AlFeO_3$ thin-film heterostructures. *ACS Appl. Electron. Mater.* **2020**, *2*, 1065−1073.
(48) Zhang, H.; F Banfield, J. Thermodynamic analysis of phase stability of nanocrystalline titania. *J. Mater. Chem.* **1998**, *8*, 2073−2076.
(49) Wang, Y.-C.; Wu, J. M. Effect of controlled oxygen vacancy on H_2-production through the piezocatalysis and piezophototronics of ferroelectric *R3c* $ZnSnO_3$ nanowires. *Adv. Funct. Mater.* **2020**, *30*, No. 1907619.
(50) Farvid, S. S.; Dave, N.; Radovanovic, P. V. Phase-controlled synthesis of colloidal In_2O_3 nanocrystals via size-structure correlation. *Chem. Mater.* **2010**, *22*, 9−11.
(51) Prewitt, C. T.; Shannon, R. D.; Rogers, D. B.; Sleight, A. W. C rare earth oxide-corundum transition and crystal chemistry of oxides having the corundum structure. *Inorg. Chem.* **1969**, *8*, 1985−1993.
(52) Sakurai, S.; Namai, A.; Hashimoto, K.; Ohkoshi, S.-i. First observation of phase transformation of all four Fe_2O_3 phases ($\gamma \rightarrow \varepsilon \rightarrow \beta \rightarrow \alpha$-Phase). *J. Am. Chem. Soc.* **2009**, *131*, 18299−18303.
(53) McHale, J. M.; Auroux, A.; Perrotta, A. J.; Navrotsky, A. Surface energies and thermodynamic phase stability in nanocrystalline aluminas. *Science* **1997**, *277*, 788.
(54) Choisnet, J.; Rulmont, A.; Tarte, P. Les tellurates mixtes Li_2ZrTeO_6 et Li_2HfTeO_6: un nouveau phénomène d'ordre dans la famille corindon. *J. Solid State Chem.* **1988**, *75*, 124−135.
(55) Choisnet, J.; Rulmont, A.; Tarte, P. Ordering phenomena in the $LiSbO_3$ type structure: The new mixed tellurates Li_2TiTeO_6 and Li_2SnTeO_6. *J. Solid State Chem.* **1989**, *82*, 272−278.
(56) Zhao, M.-H.; Wang, W.; Han, Y.; Xu, X.; Sheng, Z.; Wang, Y.; Wu, M.; Grams, C. P.; Hemberger, J.; Walker, D.; Greenblatt, M.; Li, M.-R. Reversible structural transformation between polar polymorphs of Li_2GeTeO_6. *Inorg. Chem.* **2019**, *58*, 1599−1606.
(57) Woodward, P. M.; Sleight, A. W.; Du, L.-S.; Grey, C. P. Structural studies and order−disorder phenomenon in a series of new quaternary tellurates of the type $A^{2+}M^{4+}Te^{6+}O_6$ and $A^{1+2}M^{4+}Te^{6+}O_6$. *J. Solid State Chem.* **1999**, *147*, 99−116.
(58) Kresse, G.; Joubert, D. From ultrasoft pseudopotentials to the projector augmented-wave method. *Phys. Rev. B* **1999**, *59*, 1758−1775.
(59) Perdew, J. P.; Burke, K.; Ernzerhof, M. Generalized gradient approximation made simple. *Phys. Rev. Lett.* **1996**, *77*, 3865−3868.
(60) Li, W.; Jacobs, R.; Morgan, D. Predicting the thermodynamic stability of perovskite oxides using machine learning models. *Comput. Mater. Sci.* **2018**, *150*, 454−463.
(61) Schmidt, J.; Shi, J.; Borlido, P.; Chen, L.; Botti, S.; Marques, M. A. L. Predicting the thermodynamic stability of solids combining density functional theory and machine learning. *Chem. Mater.* **2017**, *29*, 5090−5103.
(62) Krukau, A. V.; Vydrov, O. A.; Izmaylov, A. F.; Scuseria, G. E. Influence of the exchange screening parameter on the performance of screened hybrid functionals. *J. Chem. Phys.* **2006**, *125*, No. 224106.
(63) Csonka, G. I.; Perdew, J. P.; Ruzsinszky, A.; Philipsen, P. H. T.; Lebègue, S.; Paier, J.; Vydrov, O. A.; Ángyán, J. G. Assessing the performance of recent density functionals for bulk solids. *Phys. Rev. B* **2009**, *79*, No. 155107.
(64) Ye, M.; Vanderbilt, D. Domain walls and ferroelectric reversal in corundum derivatives. *Phys. Rev. B* **2017**, *95*, No. 014105.
(65) Capillas, C.; Tasci, E. S.; de la Flor, G.; Orobengoa, D.; Perez-Mato, J. M.; Aroyo, M. I. A new computer tool at the Bilbao Crystallographic Server to detect and characterize pseudosymmetry. *Z. Kristallogr.* **2011**, *226*, 186−196.
(66) Bomatí-Miguel, O.; Mazeina, L.; Navrotsky, A.; Veintemillas-Verdaguer, S. Calorimetric study of maghemite nanoparticles synthesized by laser-induced pyrolysis. *Chem. Mater.* **2008**, *20*, 591−598.
(67) Wen, H.-L.; Chen, Y.-Y.; Yen, F.-S.; Huang, C.-Y. Size characterization of θ- and α-Al_2O_3 crystallites during phase transformation. *Nanostruct. Mater.* **1999**, *11*, 89−101.
(68) Wang, L.; Zhou, F.; Meng, Y. S.; Ceder, G. First-principles study of surface properties of $LiFePO_4$: Surface energy, structure, Wulff shape, and surface redox potential. *Phys. Rev. B* **2007**, *76*, No. 165435.
(69) Miracle-Sole, S. Wulff shape of equilibrium crystals. 2013, arXiv:1307.5180. arXiv.org e-Print archive https://arxiv.org/abs/1307.5180 (accessed July 01, 2013).
(70) Rahm, J. M.; Erhart, P. WulffPack: A Python package for Wulff constructions. *J. Open Source Softw.* **2020**, *5*, 1944.
(71) Walker, D.; Carpenter, M. A.; Hitch, C. M. Some simplifications to multianvil devices for high pressure experiments. *Am. Mineral.* **1990**, *75*, 1020−1028.
(72) Walker, D. Lubrication, gasketing, and precision in multianvil experiments. *Am. Mineral.* **1991**, *76*, 1092−1100.
(73) Walker, D.; Li, J. Castable solid pressure media for multianvil devices. *Matter Radiat. Extremes* **2019**, *5*, No. 018402.
(74) Coelho, A. TOPAS and TOPAS-Academic: an optimization program integrating computer algebra and crystallographic objects written in C++. *J. Appl. Crystallogr.* **2018**, *51*, 210−218.
(75) Su, H.-P.; Li, S.-F.; Han, Y.; Wu, M.-X.; Gui, C.; Chang, Y.; Croft, M.; Ehrlich, S.; Khalid, S.; Adem, U.; Dong, S.; Sun, Y.; Huang, F.; Li, M.-R. Predicted polymorph manipulation in an exotic double perovskite oxide. *J. Mater. Chem. C* **2019**, *7*, 12306−12311.
(76) Li, M.-R.; Retuerto, M.; Stephens, P. W.; Croft, M.; Sheptyakov, D.; Pomjakushin, V.; Deng, Z.; Akamatsu, H.; Gopalan, V.; Sánchez-Benítez, J.; Saouma, F. O.; Jang, J. I.; Walker, D.; Greenblatt, M. Low-temperature cationic rearrangement in a bulk metal oxide. *Angew. Chem., Int. Ed.* **2016**, *55*, 9862−9867.
(77) Ramesh, R.; Schlom, D. G. Creating emergent phenomena in oxide superlattices. *Nat. Rev. Mater.* **2019**, *4*, 257−268.
(78) Yi, D.; Lu, N.; Chen, X.; Shen, S.; Yu, P. Engineering magnetism at functional oxides interfaces: manganites and beyond. *J. Phys.: Condens. Matter* **2017**, *29*, No. 443004.
(79) Das Sarma, S.; Deng, D.-L.; Duan, L.-M. Machine learning meets quantum physics. *Phys. Today* **2019**, *72*, 48−54.
(80) Li, M.-R.; Hodges, J. P.; Retuerto, M.; Deng, Z.; Stephens, P. W.; Croft, M. C.; Deng, X.; Kotliar, G.; Sánchez-Benítez, J.; Walker, D.; Greenblatt, M. Mn_2MnReO_6: Synthesis and magnetic structure determination of a new transition-metal-only double perovskite canted antiferromagnet. *Chem. Mater.* **2016**, *28*, 3148−3158.

(81) Arévalo-López, A. M.; Stegemann, F.; Attfield, J. P. Competing antiferromagnetic orders in the double perovskite Mn_2MnReO_6 (Mn_3ReO_6). *Chem. Commun.* **2016**, *52*, 5558−5560.
(82) Solana-Madruga, E.; Alharbi, K. N.; Herz, M.; Manuel, P.; Attfield, J. P. Unconventional magnetism in the high pressure 'all transition metal' double perovskite Mn_2NiReO_6. *Chem. Commun.* **2020**, *56*, 12574−12577.
(83) Xu, Y.; Elcoro, L.; Song, Z.-D.; Wieder, B. J.; Vergniory, M. G.; Regnault, N.; Chen, Y.; Felser, C.; Bernevig, B. A. High-throughput calculations of magnetic topological materials. *Nature* **2020**, *586*, 702−707.
(84) Dos santos-García, A. J.; Solana-Madruga, E.; Ritter, C.; Avila-Brande, D.; Fabelo, O.; Saez-Puche, R. Synthesis, structures and magnetic properties of the dimorphic Mn_2CrSbO_6 oxide. *Dalton Trans.* **2015**, *44*, 10665−10672.
(85) Aykol, M.; Dwaraknath, S. S.; Sun, W.; Persson, K. A. Thermodynamic limit for synthesis of metastable inorganic materials. *Sci. Adv.* **2018**, *4*, No. eaaq0148.
(86) Hartman, S. T.; Thind, A. S.; Mishra, R. Tin oxynitride-based ferroelectric semiconductors for solar energy conversion applications. *Chem. Mater.* **2020**, *32*, 9542−9550.
(87) Jain, A.; Ong, S. P.; Hautier, G.; Chen, W.; Richards, W. D.; Dacek, S.; Cholia, S.; Gunter, D.; Skinner, D.; Ceder, G.; Persson, K. A. Commentary: The Materials Project: A materials genome approach to accelerating materials innovation. *APL Mater.* **2013**, *1*, No. 011002.
(88) Sun, W.; Dacek, S. T.; Ong, S. P.; Hautier, G.; Jain, A.; Richards, W. D.; Gamst, A. C.; Persson, K. A.; Ceder, G. The thermodynamic scale of inorganic crystalline metastability. *Sci. Adv.* **2016**, *2*, No. e1600225.
(89) Ye, M.; Vanderbilt, D. Ferroelectricity in corundum derivatives. *Phys. Rev. B* **2016**, *93*, No. 134303.
(90) Lu, W.; Gao, Z.; Liu, X.; Tian, X.; Wu, Q.; Li, C.; Sun, Y.; Liu, Y.; Tao, X. Rational design of a $LiNbO_3$-like nonlinear optical crystal, Li_2ZrTeO_6, with high laser-damage threshold and wide mid-IR transparency window. *J. Am. Chem. Soc.* **2018**, *140*, 13089−13096.
(91) Gonschorek, W.; Feld, R. Neutron diffraction study of the thermal and oxygen position parameters in rutile. *Z. Kristallogr.* **1982**, *161*, 1−5.
(92) Yamaoka, S.; Fukunaga, O.; Ono, T.; Iizuka, E.; Asami, S. Phase transformations in Li_2WO_4 at high pressure. *J. Solid State Chem.* **1973**, *6*, 280−285.
(93) Inaguma, Y.; Yoshida, M.; Katsumata, T. A polar oxide $ZnSnO_3$ with a $LiNbO_3$-type structure. *J. Am. Chem. Soc.* **2008**, *130*, 6704−6705.
(94) Hamasaki, Y.; Shimizu, T.; Taniguchi, H.; Taniyama, T.; Yasui, S.; Itoh, M. Epitaxial growth of metastable multiferroic $AlFeO_3$ film on $SrTiO_3$ (111) substrate. *Appl. Phys. Lett.* **2014**, *104*, No. 082906.
(95) Wang, Y.; Zhang, L.; Wang, J.; Li, Q.; Wang, H.; Gu, L.; Chen, J.; Deng, J.; Lin, K.; Huang, L.; Xing, X. Chemical-pressure-modulated $BaTiO_3$ thin films with large spontaneous polarization and high Curie temperature. *J. Am. Chem. Soc.* **2021**, *143*, 6491−6497.
(96) Zhang, W.; Oganov, A. R.; Goncharov, A. F.; Zhu, Q.; Boulfelfel, S. E.; Lyakhov, A. O.; Stavrou, E.; Somayazulu, M.; Prakapenka, V. B.; Konôpková, Z. Unexpected stable stoichiometries of sodium chlorides. *Science* **2013**, *342*, 1502.
(97) Paglione, J.; Greene, R. L. High-temperature superconductivity in iron-based materials. *Nat. Phys.* **2010**, *6*, 645−658.
(98) Li, Z.; Cho, Y.; Li, X.; Li, X.; Aimi, A.; Inaguma, Y.; Alonso, J. A.; Fernandez-Diaz, M. T.; Yan, J.; Downer, M. C.; Henkelman, G.; Goodenough, J. B.; Zhou, J. New mechanism for ferroelectricity in the perovskite $Ca_{2-x}Mn_xTi_2O_6$ synthesized by spark plasma sintering. *J. Am. Chem. Soc.* **2018**, *140*, 2214−2220.
(99) Han, Y.; Zhu, C.; Peng, Y.; Li, S.; Wu, M.; Zhao, S.; Deng, Z.; Jin, C.; Du, W.; Walker, D.; Li, M.-R. Above-room-temperature $LiNbO_3$-type polar magnet stabilized by chemical and physical pressure. *Chem. Mater.* **2020**, *32*, 1618−1626.
(100) Ma, Y.; Molokeev, M. S.; Zhu, C.; Zhao, S.; Han, Y.; Wu, M.; Liu, S.; Tyson, T. A.; Croft, M.; Li, M.-R. Magnetic transitions in exotic perovskites stabilized by chemical and physical pressure. *J. Mater. Chem. C* **2020**, *8*, 5082−5091.
(101) Tokoro, H.; Tarora, W.; Namai, A.; Yoshikiyo, M.; Ohkoshi, S.-i. Direct observation of chemical conversion from Fe_3O_4 to ε-Fe_2O_3 by a nanosize wet process. *Chem. Mater.* **2018**, *30*, 2888−2894.
(102) Jiang, X. B.; Jiang, M.; Zhao, M. Thermodynamic understanding of phase transitions of In_2O_3 nanocrystals. *Chem. Phys. Lett.* **2013**, *563*, 76−79.
(103) Fujiwara, K.; Minato, H.; Shiogai, J.; Kumamoto, A.; Shibata, N.; Tsukazaki, A. Thin-film stabilization of $LiNbO_3$-type $ZnSnO_3$ and $MgSnO_3$ by molecular-beam epitaxy. *APL Mater.* **2018**, *7*, No. 022505.
(104) Fujita, T. C.; Zhang, L. F.; Kawasaki, M. Antiferromagnetic metallic state as proved by magnetotransport in epitaxially stabilized perovskite $PbRuO_3$. *Phys. Rev. Mater.* **2020**, *4*, No. 031401.
(105) Miura, K.; Fujiwara, K.; Tsukazaki, A. Growth control of corundum-derivative $MnSnO_3$ thin films by pulsed-laser deposition. *AIP Adv.* **2019**, *9*, No. 035210.
(106) Gurlo, A. Structural stability of high-pressure polymorphs in In_2O_3 nanocrystals: Evidence of stress-induced transition? *Angew. Chem., Int. Ed.* **2010**, *49*, 5610−5612.
(107) Tran, X. Q.; Hong, M.; Maeno, H.; Kawami, Y.; Toriyama, T.; Jack, K.; Chen, Z.-G.; Zou, J.; Matsumura, S.; Dargusch, M. S. Real-time observation of the thermally-induced phase transformation in GeTe and its thermal expansion properties. *Acta Mater.* **2019**, *165*, 327−335.

https://doi.org/10.1021/acs.chemmater.1c03073
Chem. Mater. 2022, 34, 186−196